Finite temperature tensor network algorithm for frustrated two-dimensional quantum materials

Philipp Schmoll,[1] Christian Balz,[2] Bella Lake,[3,4] Jens Eisert,[1,3] and Augustine Kshetrimayum[5,1,3]
[1]*Dahlem Center for Complex Quantum Systems and Institut für Theoretische Physik, Freie Universität Berlin, Arnimallee 14, 14195 Berlin, Germany*
[2]*ISIS Neutron and Muon Source, Rutherford Appleton Laboratory, Didcot OX11 0QX, United Kingdom*
[3]*Helmholtz-Zentrum Berlin für Materialien und Energie, Hahn-Meitner-Platz 1, 14109 Berlin, Germany*
[4]*Institut für Festkörperphysik, Technische Universität Berlin, Hardenbergstraße 36, D-10623 Berlin, Germany*
[5]*Theory Division, Saha Institute of Nuclear Physics, 1/AF Bidhannagar, Kolkata 700 064, India*

(Received 22 December 2022; accepted 7 May 2024; published 10 June 2024)

Aimed at a more realistic classical description of natural quantum systems, we present a two-dimensional tensor network algorithm to study finite temperature properties of frustrated model quantum systems and real quantum materials. For this purpose, we introduce the infinite projected entangled simplex operator ansatz to study thermodynamic properties. To obtain state-of-the-art benchmarking results, we explore the highly challenging spin-1/2 Heisenberg antiferromagnet on the Kagome lattice, a system for which we investigate the melting of the magnetization plateaus at finite magnetic field and temperature. Making a close connection to actual experimental data of real quantum materials, we go on to studying the finite temperature properties of $Ca_{10}Cr_7O_{28}$. We compare the magnetization curve of this material in the presence of an external magnetic field at finite temperature with classically simulated data. As the first theoretical tool that incorporates both thermal fluctuations as well as quantum correlations in the study of this material, our work contributes to settling the existing controversy between the experimental data and previous theoretical works on the magnetization process.

DOI: 10.1103/PhysRevB.109.235119

I. INTRODUCTION

Simulating complex quantum materials is considered to be one of the hardest problems in modern physics. Density functional theory is arguably the most popular approach to date for calculating the electronic structure of molecules and extended materials [1,2]. In situations in which strong correlations are expected to be dominant, however, its applicability can be limited. Ultimately, the core computational challenge in the numerical simulation of strongly correlated quantum materials arises from the exponential scaling of the size of the Hilbert space with the system size. Thus, it comes as no surprise that the *exact diagonalization* (ED) technique can only study small sizes and therefore may fail to capture the important physics of emergent many-body phenomena. Mean-field techniques are also unsuitable in the study of quantum materials as they neglect the most crucial ingredient in describing these systems: quantum entanglement. While *quantum Monte Carlo* constitutes a versatile tool for simulating unfrustrated strongly correlated systems [3], they suffer from severe limitations for frustrated quantum systems due to the sign problem. In this respect, *tensor network* techniques have emerged as a powerful alternative for studying challenging many-body problems which does not suffer from any of those limitations [4–7].

The success of one-dimensional tensor networks, also known as *matrix product states* (MPS) [8–11], in describing one-dimensional phases of matter have provided much impetus to the development of two-dimensional tensor network algorithms. While the situation is much more intricate and challenging in two spatial dimensions, such tensor network algorithms, also known as *projected entangled pair states* (PEPS) or *iPEPS* [5,12,13] in its infinite instance tackling directly the thermodynamic limit, have recently matured and have been employed successfully to study various challenging problems in two dimensions. This includes finding ground states of frustrated systems and real quantum materials [14–20] and nonequilibrium systems [21–27]. While most of the efforts has been dedicated towards identifying ground states of closed quantum systems, in order to accurately capture the physics of quantum materials in realistic conditions in the laboratory, one needs to include the effects of temperature. With this aim, there have been several recent works on two-dimensional *finite temperature tensor network algorithms* [28–35]. Most of these works have, however, focused on paradigmatic, theoretical models such as the Ising, Kitaev or Heisenberg models, and mostly models that are defined on the square lattice. Previous works on realistic two-dimensional systems using tensor networks for finite temperature mostly rely on MPO-based approaches [36–39]. These methods, while accurate and efficient, can target the thermodynamic limit of the system only along one direction.

In this work, we develop a two-dimensional tensor network algorithm in the true two-dimensional thermodynamic limit for studying finite temperature properties of existing quantum materials, thus mimicking experimental studies as closely as possible. We start by describing our method and then present results on two important instances of strongly correlated systems: (i) the paradigmatic spin-1/2 Kagome Heisenberg antiferromagnet both in the absence and presence

of an external magnetic field and (ii) the real quantum material $Ca_{10}Cr_7O_{28}$ that features a bilayer Kagome structure.

II. METHOD

Our method substantially advances the algorithm proposed in Ref. [30] by extending it to the more challenging realm of frustrated quantum systems and real quantum materials. This step renders it possible to directly compare experimental data and theoretical tensor network simulations, as we do here. We will now review the underlying annealing algorithm and highlight the improvements. In order to simulate a quantum system at finite temperature $\beta \coloneqq 1/T > 0$, we describe it by an (unnormalized) thermal quantum state

$$\rho(\beta) = \mathrm{e}^{-\beta H}, \tag{1}$$

where H is the full local many-body Hamiltonian. To obtain such a Gibbs state, we start from an infinite temperature state, i.e., $\rho(\beta = 0)$ and cool down the system to the desired temperature $\beta^{-1} > 0$. The initial state is simply a tensor product of identities, the (unnormalized) single-particle thermal state in the limit $T \to \infty$. The evolution to the desired temperature can be generated by suitably many small temperature steps $\delta\beta$, so that the full quantum state is obtained for $N \in \mathbb{N}$ by

$$\rho(\beta) = \rho(\delta\beta)^N = (\mathrm{e}^{-\delta\beta H})^N \tag{2}$$

with $\delta\beta \coloneqq \beta/N$ and $\rho(\delta\beta)$ as what we call the *infinitesimal thermal density matrix* (ITDM). This cooling is implemented by a simple update technique [30,40]. The simple update is adopted here for its numerical stability and efficiency [14,16,30,41], particularly relevant while working on systems with large physical dimensions, which seems a necessity for the demanding task considered here (see the Appendix).

Instead of directly cooling down to $\beta > 0$, it is advantageous to cool down to $\beta/2$ and evaluate the Gibbs state as

$$\rho(\beta) = \rho(\beta/2)^\dagger \rho(\beta/2). \tag{3}$$

This ensures that the resulting operator is *positive semidefinite* and hence reflects a valid quantum state, which is otherwise not guaranteed in tensor network implementations due to truncation effects [37,42,43]. Equation (3) is *the* main difference to the underlying algorithm presented in Ref. [30] and is the crucial improvement which enables the simulation of frustrated systems (along with using the correct tensor network structure of the underlying lattice of the model as we discuss in the next paragraph). Thus, we have the freedom of evolving up to only $N/2$ steps thereby saving a factor of two in the number of annealing steps or evolving up to N steps with each step size being $\delta\beta/2$. The latter choice is adopted in our simulations and decreases the Trotter error from $\mathcal{O}(\delta\beta^2)$ to $\mathcal{O}(\delta\beta^2/4)$.

We will now introduce the tensor network representation of the Gibbs state: the *infinite projected entangled simplex operator* (iPESO) shown in Fig. 1. It is the operator version of the *infinite projected entangled simplex state* (iPESS) proposed in Ref. [44], applied to the simulation of thermal density matrices. In both tensor networks, the quantum correlations inherently present on the Kagome triangles are efficiently and accurately captured by exploiting the structure of its dual, the honeycomb lattice. Green tensors represent the lattice sites of the Kagome lattice, with two physical indices for the density matrix (as opposed to a quantum state, for which tensors only have a single physical index). They are connected by purely virtual simplex tensors shown in grey. The accuracy with which the iPESO approximates the thermal density matrix is controlled by the bond dimension of the virtual bulk indices, denoted as χ_B. It is important to note that χ_B needs to be chosen sufficiently large to prevent truncation effects in the ITDM. This leads to a minimal bond dimension of p^2, where p is the dimension of the Hilbert space of the local physical degrees of freedom. For the final simulations of the targeted real material, we choose the bond dimension such that the total truncation error becomes insignificant, an extended discussion of this error is presented in the Appendix. Expectation values are then directly computed in the tensor network representation of the thermal state according to

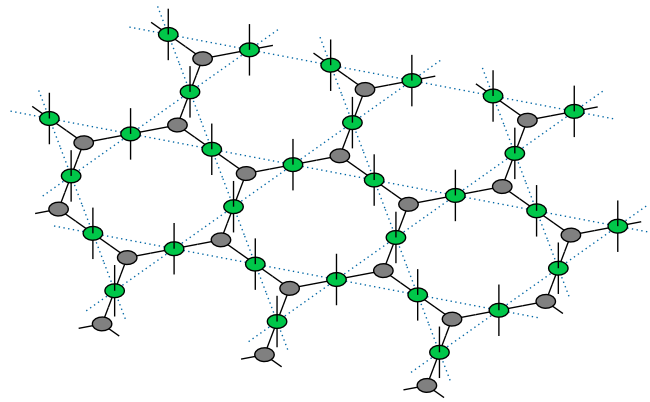

FIG. 1. iPESO ansatz for the simulation of Gibbs states on the Kagome lattice (shown in light blue).

$$\langle \hat{O} \rangle = \frac{1}{N_\rho} \mathrm{Tr}[\rho(\beta/2)^\dagger \, \hat{O} \, \rho(\beta/2)], \tag{4}$$

with a normalization factor $N_\rho \coloneqq \mathrm{Tr}[\rho(\beta/2)^\dagger \, \rho(\beta/2)]$. Expectation values can be computed by either using the simple update mean-field environment, or by a full *corner transfer matrix renormalization group (CTMRG)* procedure [45–47], which captures quantum correlations more faithfully. For the latter, the environment bond dimension χ_E controls the approximations in the contraction of the infinite two-dimensional lattice. Details for both the simple update cooling and calculations of expectation values are presented in detail in the Appendix. Compared to the basic algorithm in Ref. [30], the iPESO simple update is computationally more efficient with a leading cost of $\mathcal{O}(d^8\chi_B^4)$ in contrast with $\mathcal{O}(d^4\chi_B^5 + d^{12}\chi_B^3)$. Due to the preservation of the positivity of the thermal state, our double-layer CTMRG approach scales as $\mathcal{O}(d^2\chi_B^6\chi_E^2 + \chi_B^6\chi_E^3)$. The smallest possible unit cell of the iPESO consists of three lattice site tensors and two simplex tensors, as presented in Fig. 1. Besides this structure, we also employ a nine-site unit cell in our numerical simulation. This is required to capture thermal states with larger structures that are not commensurate with three-site translational invariance.

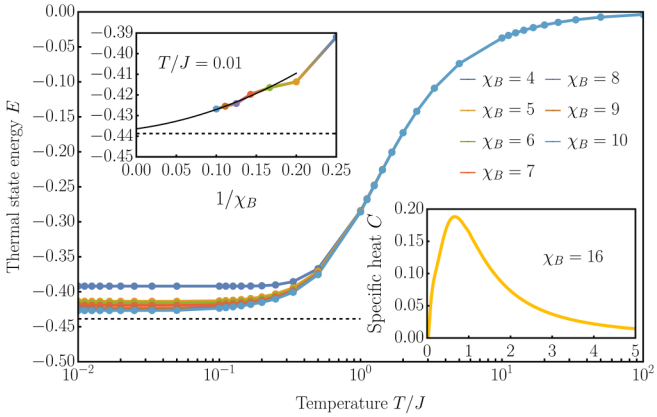

FIG. 2. Thermal state energy for the spin-1/2 Heisenberg model on the Kagome lattice at various bulk bond dimensions χ_B, using CTMRG environments. The dashed line corresponds to the $T/J = 0$ ground state energy of Ref. [54]. (Top inset) Convergence of the thermal state energy with inverse bond dimension at $T/J = 0.01$. (Bottom inset) Specific heat C at $\chi_B = 16$, using mean-field environments.

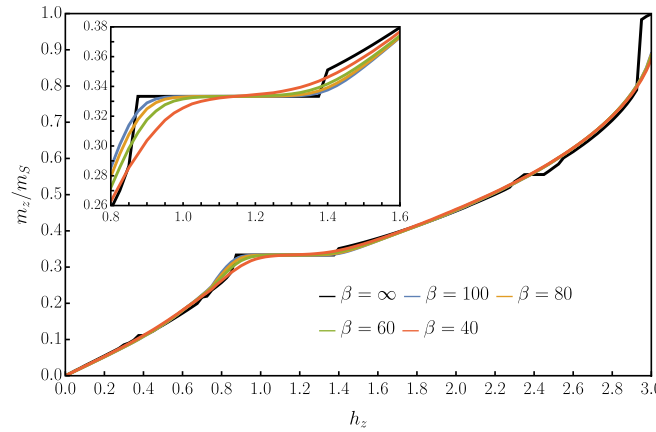

FIG. 3. Magnetization of the Kagome Heisenberg antiferromagnet over magnetic fields h_z for various temperatures T/J. Additionally, we show the $T = 0$ magnetization curve obtained via iPESS simulations in black. (Inset) Melting of the $m_z/m_S = 1/3$ plateau.

III. MODELS AND RESULTS

A. Kagome Heisenberg antiferromagnet

The first application of the developed iPESO method is the finite temperature study of the frustrated spin-1/2 Heisenberg antiferromagnet on the Kagome lattice, a paradigmatic model that has been a topic of intense study in the community [14,48–53]. Its Hamiltonian is given by

$$H = J \sum_{\langle i,j \rangle} \vec{S}_i \cdot \vec{S}_j - h_z \sum_i S_i^z, \tag{5}$$

where $\vec{S}_i$ are spin-1/2 operators on site i and $\langle i, j \rangle$ denotes nearest-neighbours in the underlying lattice, h_z is a magnetic field applied along the z-axis. In the following, we employ the iPESO method to study the model at $J = 1.0$ over a large temperature range, choosing an infinitesimal temperature step $\delta\beta = 10^{-3}$. In the main panel of Fig. 2, we show the thermal state energy for a three-site iPESO ansatz at bulk bond dimensions up to $\chi_B = 10$. These results are computed using a CTMRG procedure with individual environment bond dimensions χ_E such that expectation values are well converged at least up to three significant digits. The other source of error is in the truncation of the simple update cooling procedure, which corresponds to the amount of information that is discarded to keep the bond dimension of the iPESO fixed for practical reasons. In our simulation, we balance all refinement parameters such that the overall truncation error stays below $\varepsilon \sim 1 \times 10^{-2}$. A detailed discussion of this error is provided in the Appendix. The energy of the thermal state approaches the ground state energy at $T = 0$ for low temperatures, as shown in the top inset. A second order polynomial fit of $E(1/\chi_B)$ provides further indication, that the annealing procedure does not get stuck in local minima and flows towards the correct ground state as would have been obtained using direct ground state optimization techniques in the infinite bond dimension limit. While the thermal state energies in Fig. 2 have been computed with CTMRG environments, we note that the accuracy is not affected while using the mean-field environment of the simple update. Therefore we compute the *heat capacity* $C := \partial U/\partial T$ at a higher bulk bond dimension $\chi_B = 16$, using these environments. The result is shown in the bottom inset and matches previous finite temperature studies of the model [43]. For further analysis of the model and for the target real material, we therefore use mean-field environments, since CTMRG calculations are limited to inexpressively small environment bond dimensions in these cases.

We further use our method to study the effect of temperature on the magnetization behavior of the Heisenberg model in Eq. (5). It is known that different magnetization plateaus at values $m_z/m_S = [1/9, 1/3, 5/9]$ of the saturation magnetization $m_S = 1/2$ appear at $T/J = 0$ upon tuning the magnetic field h_z [15,17]. Those plateaus are correctly recovered when employing $T/J = 0$ iPESS simulations. At finite temperature, we simulate the Kagome Heisenberg model in a field using a nine-site iPESO at bond dimension $\chi_B = 12$. Figure 3 reports the magnetization for various temperatures. Of all the $T/J = 0$ magnetization plateaus, we find that only the $m_z/m_S = 1/3$ plateau survives at finite temperature up to $T/J \sim 2 \times 10^{-2}$. Above this temperature, the plateau starts melting and disappears. We therefore focus our study on this most prominent 1/3 magnetic plateau in the figure inset. The chosen constant temperature slices of $1/(T/J) = [\infty, 100, 80, 60, 40]$ reveal, that the melting is stronger at the low-field end of the plateau. This is in good agreement with a recent exact diagonalization study of the melting of the magnetization plateaus [55,56]. Our results serve as an important guide to the experimental study of the magnetization process of closely related real materials such as Herbertsmithite $ZnCu_3(OH)_6Cl_2$ and its relatives.

B. Real material $Ca_{10}Cr_7O_{28}$

The material $Ca_{10}Cr_7O_{28}$ has a breathing bilayer Kagome structure, with alternating ferro- and antiferromagnetic

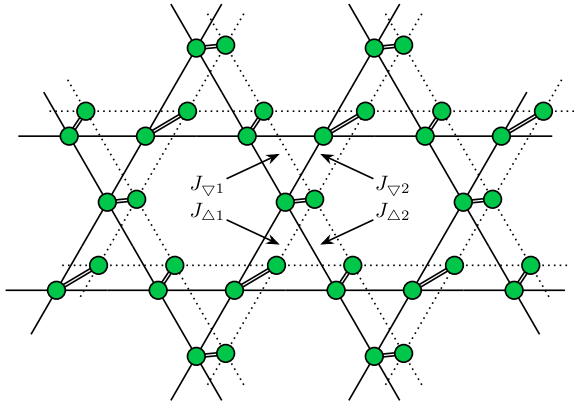

FIG. 4. Breathing bilayer Kagome lattice with different couplings for the compound material $Ca_{10}Cr_7O_{28}$. The double bonds denote interlayer coupling with coupling strength J_{inter}.

Heisenberg interactions on neighboring triangles, defined by

$$H = \sum_{k=1}^{2} \left[J_{\nabla k} \sum_{\langle i,j \rangle} \vec{S}_i \cdot \vec{S}_j + J_{\triangle k} \sum_{\langle i,j \rangle} \vec{S}_i \cdot \vec{S}_j \right] + J_{\text{inter}} \sum_{\langle i,j \rangle} \vec{S}_i \cdot \vec{S}_j - h_z \sum_i S_i^z, \tag{6}$$

where $J_{\nabla k}$ and $J_{\triangle k}$ are the intra-Kagome couplings in the two layers $k = 1$ and $k = 2$ while J_{inter} denotes the coupling between the two layers. The lattice structure is shown in Fig. 4. The different coupling parameters have been determined from neutron scattering experiments of the real material in Ref. [57]. These values (in meV) are $J_{\nabla 1} = +0.09(2)$, $J_{\triangle 1} = -0.27(3)$, $J_{\nabla 2} = -0.76(5)$, $J_{\triangle 2} = +0.11(3)$ and $J_{\text{inter}} = -0.08(4)$, where the numbers in round brackets indicate the uncertainties.

The bilayer Kagome structure can be mapped to a single layer by combining the two spins in the different layers to a single physical site, so that a regular iPESO ansatz with an enlarged local physical dimension of $d = 4$ can be used. The large physical dimension of the system also means that the minimum bond dimension required for accurate simulations of the material needs to be sufficiently high ($\chi_B \geqslant 16$). This becomes a bottleneck in computing expectation values using CTMRG routines. For this reason, we have adopted the mean-field environment calculation which takes into account the quantum correlations within a cluster. We find that even with such approximations in computing the magnetization and heat capacity, our results are compatible with the experimental data and provide novel insights into the earlier discrepancy between theory and experiment data as we show below. For a detailed discussion of the numerical errors in the simulation of the bilayer material, we refer to the Appendix.

1. Magnetization behaviour

The magnetic properties of this real material have been investigated previously at zero temperature using tensor networks and compared to experimental measurements by some of the current authors [19]. While results at small magnetic fields were in good agreement, the magnetization curve shows

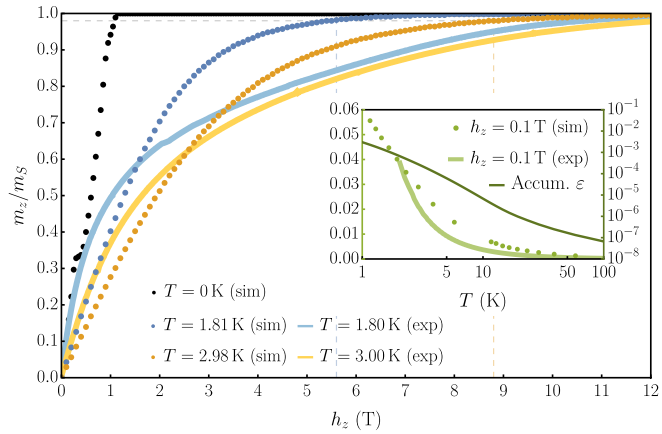

FIG. 5. Magnetization curve of $Ca_{10}Cr_7O_{28}$ for the Hamiltonian given in Eq. (6) and magnetic fields between 0 and 12 T at different temperatures at $\chi_B = 30$. With decreasing temperature, the slope increases and the magnetization saturates earlier. Dashed lines are guides to the eye, showing the saturation threshold (gray) as well as corresponding magnetic field values for both simulated temperatures. The inset shows the magnetization at fixed field of $h_z = 0.1$ T as a function of temperature, using $\chi_B = 48$ to reduce simulation errors at this small scale. The accumulated truncation error ε (right axis) is shown to be insignificant for the full temperature range.

a significant discrepancy between simulation and experiment at large values of the field. Such a discrepancy has also been observed when comparing the experimental data to theoretical mean-field calculations [57]. The experimental data, which was measured at $T = 1.8$ and 3.0 K, show that the magnetization of this material increases rapidly for small external magnetic fields up to 2 T, above which the slope flattens and saturation is achieved for a field value of approximately 12 T. In contrast, the previous tensor network simulation at $T = 0$ K predicted saturation at a much smaller value of the external magnetic field of approximately 1 T. This theoretical investigation, while quantum, has ignored thermal fluctuations. For comparison, classical Monte Carlo simulations which take temperature effects into account, result in a better qualitative agreement [58]. These simulations, which were performed at the same temperatures as the experimental measurements, predict the general observed suppression of magnetization at low fields (see Fig. 13 of Ref. [58]). However, they overestimate the suppression of magnetization at higher fields with the magnetization far from saturation even at a field of 14 T. This might be because the quantum fluctuations are ignored by this method. Our present technique encompasses both the quantum properties of the material as well as the effect of finite temperature.

We now investigate the quantum material $Ca_{10}Cr_7O_{28}$ in the presence of magnetic fields between 0 and 12 T at different temperatures. The TN simulations are done with a nine-site iPESO at bond dimension $\chi_B = 30$ and with $\delta\beta = 10^{-2}$, results are shown in Fig. 5. Our theoretical results are plotted for temperatures $T = 1.81$ K and 2.98 K. This is then compared against the experimental data measured at $T = 1.8$ and 3.0 K. The conversion factors between the theoretical calculations and experiment are shown in the Appendix. From the plots in Fig. 5, we see that as we increase the temperature, the field

value at which the magnetization saturates becomes larger and approaches the experimental findings. Overall, we find that the magnetization curve shows a strong dependence on the temperature and the saturation sets in quicker for low T. This seems to indicate that the earlier discrepancy between theory and experimental data has been largely due to neglecting finite temperature effects in the theory simulations. For comparison, we show the $T = 0\,\mathrm{K}$ magnetization curve obtained with a nine-site iPESS at $\chi_B = 24$ with mean-field environments.

In order to quality the saturation behavior and compare against previous simulations, we declare saturation for a magnetization value above $m_z/m_S = 0.98$ (gray dashed line in Fig. 5). Our current TN simulations show that saturation is achieved at $h_z \approx 5.6\,\mathrm{T}$ for $T = 1.8\,\mathrm{K}$ and $h_z \approx 8.8\,\mathrm{T}$ for $T = 3.0\,\mathrm{K}$. In the experimental data saturation is reached at $h_z \approx 10.6\,\mathrm{T}$ and $h_z \approx 12.2\,\mathrm{T}$ (outside the plotting region) for the two temperature values. As expected, the agreement improves with increasing temperature. Previous classical Monte Carlo simulations did not reach saturation even at the highest field of $h_z = 14\,\mathrm{T}$, at which the magnetization was calculated to be $m_z/m_S \approx 0.84$ and ≈ 0.75, respectively. To set this in comparison, our TN simulations reach those values at $h_z = 2.8$ and $3.5\,\mathrm{T}$, and the experimental data at $h_z = 5.5$ and $4.2\,\mathrm{T}$, respectively. Therefore the TN simulations outperform the classical Monte Carlo in predicting the magnetization, because they take into account both the quantum and thermal effects.

Inelastic neutron scattering has previously revealed that the spin liquid ground state of this material is destroyed by a magnetic field of $1\,\mathrm{T}$ [57]. However, heat capacity measurements could show that magnetic fields of up to $0.5\,\mathrm{T}$ leave the spin liquid ground state intact as indicated by featureless C/T curves [57]. To check that the effect of small fields is correctly captured by our model, we have computed the magnetization as a function of temperature at fixed field strength $h_z = 0.1\,\mathrm{T}$ and contrasted it with measured experimental data. Since the ground state is still expected to be in the gapless spin liquid phase at $h_z = 0.1\,\mathrm{T}$, we use a 60 % higher bond dimension of $\chi_B = 48$ to increase accuracy and reduce simulation errors. The comparison is shown in the inset of Fig. 5, and the model indeed reproduces the experimental curve without any anomalies that would indicate a phase transition into a magnetically ordered ground state. The larger bond dimension reduces the error to a maximal value of $\varepsilon \approx 0.003$ at the lowest temperature $T = 1\,\mathrm{K}$. This confirms the accuracy of our method even for intricate phases and small computed quantities. The small discrepancy between experimental data and simulation is examined below.

2. *Heat capacity and entropy*

Finally, we compute the magnetic heat capacity from the thermal state energy U according to $C := \partial U/\partial T$ for two different values of the magnetic field $h_z = 2.0$ and $3.0\,\mathrm{T}$ and compare it with the experimental data. Results are shown in Fig. 6. The conversion factors between the theoretical calculations and experiment are again shown in the Appendix. As well as the heat capacity data, we have also computed the thermodynamic entropy by integrating the heat capacity. This is shown in the inset of Fig. 6. We find good agreement between our theoretical predictions and experimental data.

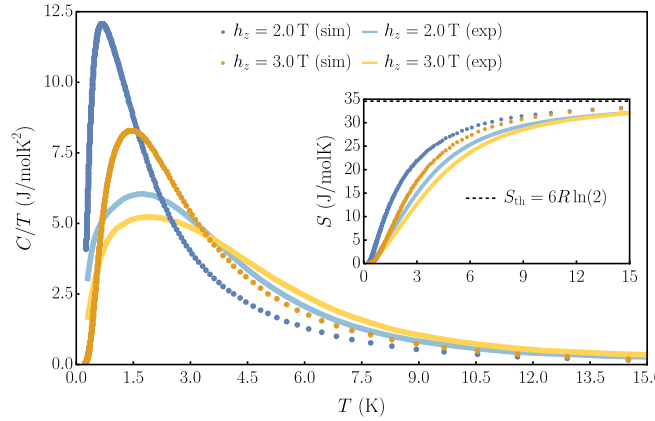

FIG. 6. Magnetic heat capacity C/T as a function of temperature for different strengths of the magnetic fields h_z. Integrating this quantity over T yields the entropy, which accurately approaches the theoretical value of $S_{\mathrm{th}} = 6R\ln(2)$, with R the ideal gas constant.

The heat capacity of $Ca_{10}Cr_7O_{28}$ at intermediate fields is characterized by a broad and smooth peak of a Schottky anomaly due to the excitations that become gapped by the magnetic field. The position of this peak shifts to higher temperature with increasing field both in the model and the experimental data. This is in qualitative agreement with an increasing gap due to the Zeeman term in the Hamiltonian, see Eq. (6). Integrating C/T to obtain the magnetic entropy shows that the model does well in capturing the total possible entropy for spin-1/2 over the temperature range up to 15 K.

3. *Implications for cross-benchmarking*

The results presented here have implications for the task of cross-benchmarking classical simulations and quantum experiments. We see our work as a contribution to the line of thought of co-evolving increasingly accurate tensor network based classical simulations and quantum experiments and simulations. This approach can be traced back to Ref. [59] and possibly even earlier work, in which results from a dynamical quantum simulations were compared to state-of-the-art findings from tensor network simulations. Such efforts have taken center stage in particular in the context of computational quantum advantage of quantum random sampling [60], where tensor network methods have been able to approximate the distributions of the original quantum experiment to good accuracy [61,62]. Similarly, tensor network methods have been used [63–65] to successfully simulate and cross benchmark quantum simulations in two spatial dimensions probing a kicked Ising system [66]. This development in the field of quantum simulation is increasingly reflected in the context of condensed matter physics. It is a major motivation of this work to contribute to the line of thought of developing tensor network methods substantially further, so that they are able to capture aspects of condensed matter experiments quantitatively [19,67,68]. It is such a cross-benchmarking effort that advances both fields and allows to build confidence in the correctness of the analysis: We believe that only if numerical

techniques are developed in parallel with the solid-state synthesis of interacting quantum many-body systems, then high levels of predictive power can be reached.

IV. CONCLUSIONS AND OUTLOOK

In this work, we have presented a two-dimensional tensor network algorithm for studying finite temperature properties for the highly challenging realm of frustrated systems and two-dimensional quantum materials. We achieve this by introducing the infinite projected entangled simplex operator algorithm. Our algorithm explicitly preserves the positive semidefiniteness of the Gibbs state represented by the iPESO. We use our technique to benchmark against finite temperature properties of the well-known, paradigmatic model of the spin-1/2 Kagome Heisenberg antiferromagnet and obtain very competitive state-of-the art results for the thermal state energy and heat capacity. We also study the melting of the magnetization plateaus of this model in the presence of external magnetic field at finite temperature. By focusing on the most prominent 1/3 plateau, we find that it starts melting and disappears at temperature $T \sim 2 \times 10^{-2}$. Moreover, the plateau starts melting from the lower end of the field, an observation that was also made recently in an independent exact diagonalization study [55].

Finally, we have investigated the finite temperature properties of the quantum material $Ca_{10}Cr_7O_{28}$ using our tensor network technique. This is particularly important due to a recent discrepancy in the magnetization process predicted by theoretical simulations compared to experimental findings. As a first theoretical study of this real material that includes both quantum correlations and finite temperature effects, we find a strong temperature dependence of the magnetization curve of this material in the presence of an external magnetic field. We find that on systematically increasing the temperature, our theoretical simulations approach the experimental data which was collected at finite temperature. We provide a direct comparison of the theoretical magnetization data with the experimental data at $T = 1.8$ and 3.0 K and find them to be in surprisingly good but not quite perfect agreement. We also computed the magnetic heat capacity (C/T) as a function of temperature at different field strengths $h_z = 2.0$ and 3.0 T as well as the entropy S. For all these quantities, we find good agreement with the experimental data.

One can argue that the agreement is striking, given that the Hamiltonian in Eq. (6) has only been recovered by neutron scattering techniques to finite precision considering five Heisenberg interactions, while Dzyaloshinskii-Moriya interactions have been excluded. Furthermore, there are truncation errors in the classical simulation. One can argue that the present analysis allows to cross-benchmark quantum experiments with classical simulations. The findings can also be seen as an invitation, however, to use high-precision tools of *Hamiltonian learning* to better identify the actual underlying microscopic Hamiltonian, given data from Gibbs states [69,70], possibly even based on tensor networks akin the approach taken in Ref. [71]. These steps would further contribute to an engineering perspective of studying realistic strongly correlated quantum materials with tensor networks.

We believe our work to be an important step towards bridging the gap between theoretical simulations and experimental studies of quantum materials, and towards providing method development increasing the predictive power of such studies. It would be straightforward to extend our algorithm to other lattices and geometries that may suit other quantum materials. By incorporating both quantum correlations and finite temperature effects, we have now made direct comparison between experimental and theoretical data possible.

ACKNOWLEDGMENTS

The authors are thankful for discussions with Ji-Yao Chen, Dante Kennes, Corinna Kollath, David Luitz, Jan Naumann, Román Orús, Matteo Rizzi and Anne-Maria Visuri. The authors would like to thank the HPC Service of ZEDAT, Freie Universität Berlin, for computing time [72]. The FUB team acknowledges funding by the European Research Council (DebuQC), the Deutsche Forschungsgemeinschaft (CRC 183 on "Entangled states of matter" and FOR 2724 on 'Thermal machines in the quantum world'), the Helmholtz Association, and the Bundesministerium für Bildung und Forschung (MUNIQC-ATOMS), for which this work constitutes method development and the Quantum Flagship (PasQuans2). B.L. acknowledges the support of Deutsche Forschungsgemeinschaft through Project No. B06 of SFB 1143 on "Correlated magnetism: From frustration to topology" (ID 247310070).

APPENDIX A: DETAILS OF THE TENSOR NETWORK ALGORITHM

1. Simple update

The simple update describes an efficient, yet approximate scheme to do the annealing respectively the imaginary time evolution of the initial density matrix. It essentially implements the evolution in Eq. (A2) together with a local truncation to keep the bulk bond dimension fixed. Without the loss of generality, we consider a Hamiltonian with local interactions in the form of

$$H = H_{\bigtriangledown} + H_{\bigtriangleup}, \tag{A1}$$

where $H_{\bigtriangledown}$ and $H_{\bigtriangleup}$ are three-spin interactions on the two types of triangles of the Kagome lattice, respectively. Making use of a first-order *Suzuki-Trotter decomposition*, the imaginary time evolution to evolve the thermal density matrix $\rho(\beta) \to \rho(\beta + \delta\beta)$ can be approximated by applying the operator

$$\begin{aligned} U(\delta\beta) &= \mathrm{e}^{-\delta\beta H_{\bigtriangledown}} \mathrm{e}^{-\delta\beta H_{\bigtriangleup}} + O(\delta\beta^2) \\ &\approx U_{\bigtriangledown}(\delta\beta) U_{\bigtriangleup}(\delta\beta) \end{aligned} \tag{A2}$$

to both three-site configurations in the tensor network. In Fig. 7, we illustrate the evolution of the iPESO with the three-body gate $U_{\bigtriangledown}(\delta\beta)$. This step involves three lattice tensors, as well as the simplex tensor $\bigtriangledown$. After the gate has been contracted with the tensors, a *higher-order singular value decomposition* (HOSVD) with subsequent truncation is used to separate the network back into simplex and lattice tensors. Since the truncation is based only on the singular values for the three indices, it is purely local. In a similar fashion, the simplex $\bigtriangleup$ is updated alongside the three lattice site tensors

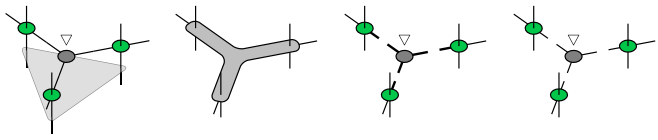

FIG. 7. Simple update step for the (imaginary) time evolution of the iPESO ansatz. After applying the three-body gate to the physical indices, a truncated higher-order SVD is used to decompose the nine-index tensor and restore the lattice and simplex tensors.

by applying the three-body gate $U_{\triangle}(\delta\beta)$. After both steps have been performed, we obtain the thermal density matrix $\rho(\beta+\delta\beta)$, represented by a three-site iPESO. This process is repeated for a fixed number of steps, such that the final thermal density matrix represents the quantum system at the desired (inverse) temperature. Naturally, this can be extended to Hamiltonians with less or more than three-site interactions. Additionally, physical symmetries of the Hamiltonian [like U(1) or SU(2)] can be readily directly incorporated, exploiting symmetry-preserving tensors [73,74].

2. Bond dimension considerations

As it is common in tensor network applications, the bond dimension controls the precision of the simulations. Here, we aim at presenting a discussion of the minimal bond dimensions required in order to obtain meaningful results. The infinitesimal thermal density matrix

$$\rho(\delta\beta) = \prod_{\langle i,j,k\rangle} \mathrm{e}^{-\delta\beta H_{i,j,k}} + \mathcal{O}(\delta\beta^2), \tag{A3}$$

here to first order in the Suzuki-Trotter decomposition, can be constructed by applying the Trotterized Hamiltonian gates $\exp(-\delta\beta H_{i,j,k})$ onto the infinite temperature Gibbs state $\rho(\beta=0)$, as shown in Fig. 8 (the infinite temperature state is simply a tensor product of identity matrices). An accurate representation (within the inevitable Trotter error) of this state is only possible if the resulting iPESO tensors are not truncated. Since the infinite temperature state has a bond dimension of unity, the infinitesimal thermal density matrix necessarily has bond dimension p^2, where p is the physical dimension of the system. Naturally, cooling the state down to lower temperatures can only produce meaningful results, if the bond dimension is larger than the minimally necessary one.

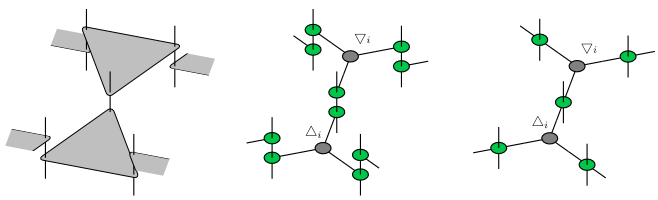

FIG. 8. Construction of the infinitesimal thermal density operator $\rho(\delta\beta)$ by a decomposition of the Trotter gates [see Eq. (A2)]. An exact representation (apart from the inevitable Trotter error) can only be achieved without truncating the virtual bulk bond dimension, which is therefore at least p^2.

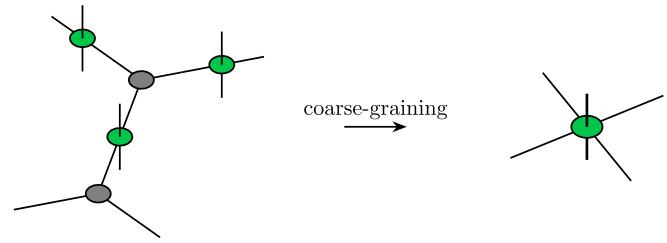

FIG. 9. Coarse-graining of a three-site iPESO into a single-site iPEPO tensor. For larger iPESO unit cells the resulting iPEPO network will have a larger unit cell, too.

3. Effective environments and expectation values

In order to evaluate physical observables and compute expectation values accurately, the infinite two-dimensional iPESO tensor network needs to be contracted. It is known that this task cannot be performed exactly classically efficiently both in worst case and average case complexity [75,76], without an exponential increase in computation time, so that approximate methods must be employed. Here we utilize the so-called *corner transfer matrix renormalization group* (CTMRG) to compute the effective environment tensors for every lattice site. To this end, we coarse-grain the iPESO network to an iPEPO network, the operator form of the famous *infinite projected entangled pair state* (iPEPS), as visualized in Fig. 9. After coarse-graining, the environment surrounding each local thermal density matrix can be conveniently computed using a standard CTMRG procedure. To this end, the contraction of the infinite square lattice is approximated by a set of fix-point environment tensors, as shown in Fig. 10. This enables both accurate calculations of expectation values and would be essential in devising a sophisticated update procedure that includes all quantum correlations in the system—the so-called *full update* [22,77]. Since the two physical indices are traced over, the procedure is a straightforward extension of a regular CTMRG routine for a two-dimensional iPEPS wave function. In order to ensure that the thermal density matrix is reflected by a positive semidefinite operator, a double-layer approach is taken in contrast to the original proposal in Ref. [30].

APPENDIX B: EFFECT OF DIFFERENT UNIT CELL SIZES

In order to test the simple update cooling procedure on different unit cells, we simulated the regular Kagome Heisenberg AF using a three-, six-, and nine-site iPESO. While a three-site ansatz is natural to capture the fully translational

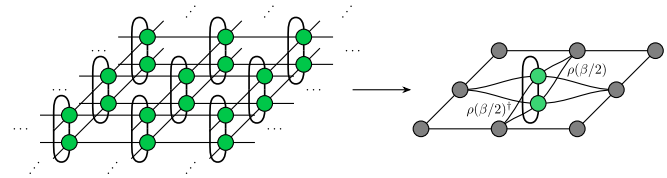

FIG. 10. A directional CTMRG routine is used to approximate the contraction of the infinite square lattice by a set of fixed-point environment tensors, denoted in grey.

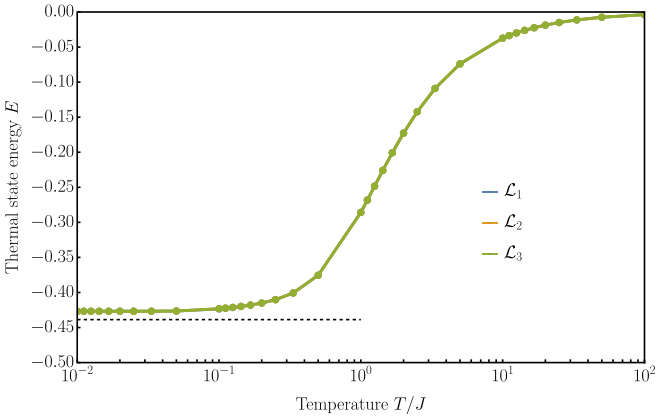

FIG. 11. Convergence of the thermal state energy with temperature for the Kagome Heisenberg AF. Simulations are performed at a fixed bond dimension $\chi_B = 10$ for different sizes of the iPESO unit cell, using CTMRG environments to compute expectation values.

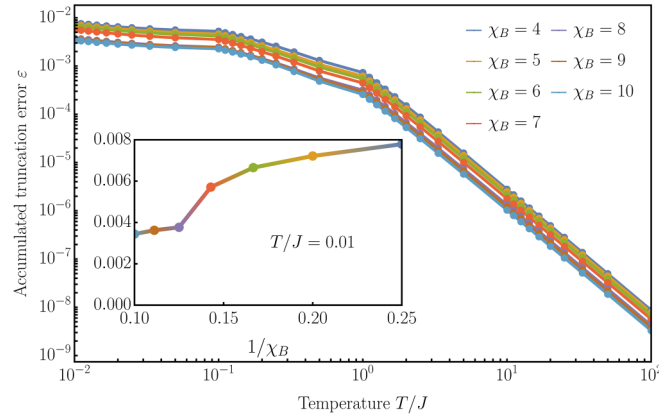

FIG. 12. Accumulated truncation error in the simple update annealing for the AF Heisenberg model on the Kagome lattice for $\delta\beta = 10^{-3}$. The inset shows the truncation error at the lowest temperature over the inverse bond dimension.

and rotational invariant spin-liquid ground state, cooling a larger unit cell reveals the method's tendency to break lattice symmetries. Using a bulk bond dimension of $\chi_B = 10$, we employed unit cells

$$\mathcal{L}_1 = (A), \quad \mathcal{L}_2 = \begin{pmatrix} A & B \\ B & A \end{pmatrix}, \quad \mathcal{L}_3 = \begin{pmatrix} A & B & C \\ B & C & A \\ C & A & B \end{pmatrix} \tag{B1}$$

on the coarse-grained square lattice, where each iPEPO tensor incorporates three lattice sites of the iPESO on the honeycomb lattice. Results for the thermal state energy over temperature are shown in Fig. 11. The thermal state energies of the three unit cells agree to at least three significant digits over the full range of temperatures. Moreover, starting from a fully translationally invariant infinite temperature state of local identities, the cooling procedure does not break the lattice symmetry, which has been checked by computing the spatial pattern of spin-spin correlations. This shows that our procedure gives consistent results for different sizes of the unit cell.

1. Truncation errors in the cooling procedure

The annealing scheme adopted in this study is based on the simple update, which requires truncations in order to keep the bulk bond dimension χ_B constant. Moreover, the choice of the infinitesimal cooling step $\delta\beta$ controls the unavoidable error in the Trotterization, and the number of annealing steps which include a truncation. The simple update is the main source of errors in the numerical procedure, since it generates the thermal density matrix $\rho(\beta)$ in the first place. For the calculations of CTMRG expectation values, a high enough environment bond dimension χ_E ensures that truncation effects can be neglected. For mean-field expectation values, the singular values of the simple update again determine the accuracy. In order to get an estimate of the overall cooling error, we compute the accumulated truncation error ε, given by the vector norm of the discarded singular values of all simple update annealing steps.

For the thermal state simulation of the Kagome Heisenberg antiferromagnet, we choose a small temperature step $\delta\beta = 10^{-3}$. In Fig. 12, we show the accumulated truncation error over temperature for various bond dimensions. At lowest temperature of $T/J = 0.01$ the truncation error is not yet fully converged, however, it stays well below $\varepsilon = 1 \times 10^{-2}$ for the largest bond dimension $\chi_E = 10$.

For the thermal state simulations of $Ca_{10}Cr_7O_{28}$ we choose a cooling step size of $\delta\beta = 10^{-2}$. In Fig. 13 we show the thermal state energy E over temperature T for several values of the magnetic fields, at which we compare our simulations to experimental findings. For $h_z = 0.1$ T, where the system is expected to be in the gapless spin liquid phase, we choose higher bond dimensions to reduce simulation errors. The thermal state energy converges very well with temperature and approaches the value of the true ground state energy in the limit $T \to 0$ K, simulated by iPESS at $\chi_B = 24$. The agreement of simulations at different bond dimensions, and as well with the ground state energy as $T \to 0$ gets better with increasing magnetic field. This is expected, since at small values of the

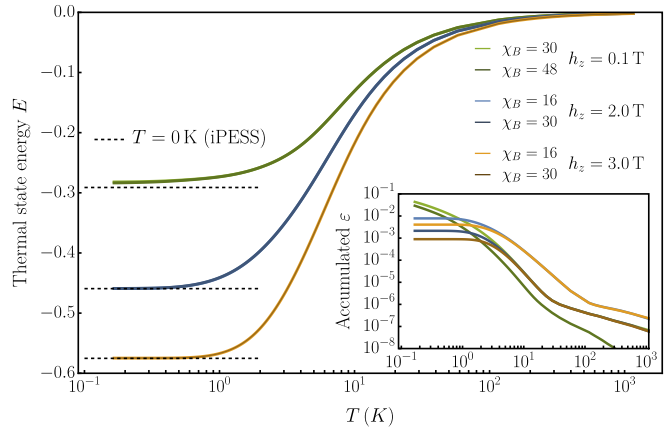

FIG. 13. Convergence of the thermal state energy with bond dimension χ_B and temperature T for several magnetic field strengths considered in our study. The inset shows the accumulated truncation error ε as a measure of numerical errors in the cooling procedure. Dashed lines correspond to $T = 0$ K iPESS ground state energies.

field, the low temperature states are closer to the highly entangled spin-liquid ground state of the material at $h_z = 0\,\mathrm{T}$ and therefore, require higher bond dimension for their simulation. This is also supported by the inset showing the accumulated truncation error for the same simulation parameters, that all stay below $\varepsilon \sim 5 \times 10^{-2}$. At the temperatures where we compare with experimental data, the truncation errors even stay below $\varepsilon = 1 \times 10^{-2}$.

APPENDIX C: CONVERSION BETWEEN EXPERIMENT AND SIMULATION

In order to compare the simulated tensor network data with measured experimental data, we need to apply the correct conversion factors. Since the coupling constants in the Hamiltonian are given in units of meV and we set $k_B = 1$, the temperature T_{sim} is in meV, too. The proper conversion to K is, therefore, given by

$$\frac{T_{\mathrm{exp}}}{T_{\mathrm{sim}}} = \frac{1\,\mathrm{meV}}{k_B} = \frac{1.602 \times 10^{-22}\,\mathrm{J}}{k_B} \approx 11.6\,\mathrm{K}. \tag{C1}$$

Furthermore, we need to convert the heat capacity C between simulated and measured data. The tensor network data is given per spin in units of $\mathrm{meV\,K^{-1}}$. In order to convert it, a factor of

$$\frac{C_{\mathrm{exp}}}{C_{\mathrm{sim}}} = 6 \cdot 1.602 \times 10^{-22}\,\mathrm{J} \cdot N_A \approx 578.8\,\mathrm{J\,mol^{-1}} \tag{C2}$$

with $N_A = 6.022 \times 10^{23}\,\mathrm{mol^{-1}}$ the Avogadro constant, is required. The additional factor of six stems from the fact, that one formula unit of $Ca_{10}Cr_7O_{28}$ has six spin-1/2 chromium ions.

[1] W. Kohn and L. J. Sham, Self-consistent equations including exchange and correlation effects, Phys. Rev. **140**, A1133 (1965).

[2] A. Tkatchenko and M. Scheffler, Accurate molecular van der waals interactions from ground-state electron density and free-atom reference data, Phys. Rev. Lett. **102**, 073005 (2009).

[3] F. Becca and S. Sorella, *Quantum Monte Carlo Approaches for Correlated Systems* (Cambridge University Press, Cambridge, 2017).

[4] R. Orús, A practical introduction to tensor networks: Matrix product states and projected entangled pair states, Ann. Phys. **349**, 117 (2014).

[5] F. Verstraete, J. I. Cirac, and V. Murg, Matrix product states, projected entangled pair states, and variational renormalization group methods for quantum spin systems, Adv. Phys. **57**, 143 (2008).

[6] J. C. Bridgeman and C. T. Chubb, Hand-waving and interpretive dance: An introductory course on tensor networks, J. Phys. A **50**, 223001 (2017).

[7] J. Eisert, M. Cramer, and M. B. Plenio, Area laws for the entanglement entropy, Rev. Mod. Phys. **82**, 277 (2010).

[8] S. R. White, Density matrix formulation for quantum renormalization groups, Phys. Rev. Lett. **69**, 2863 (1992).

[9] U. Schollwöck, The density-matrix renormalization group, Rev. Mod. Phys. **77**, 259 (2005).

[10] U. Schollwöck, The density-matrix renormalization group in the age of matrix product states, Ann. Phys. **326**, 96 (2011).

[11] D. Perez-Garcia, F. Verstraete, M. M. Wolf, and J. I. Cirac, Matrix product state representations, Quantum Inf. Comput. **7**, 401 (2007).

[12] F. Verstraete and I. Cirac, Renormalization algorithms for quantum-many body systems in two and higher dimensions, arXiv:cond-mat/0407066.

[13] J. Jordan, R. Orus, G. Vidal, F. Verstraete, and J. I. Cirac, Classical simulation of infinite-size quantum lattice systems in two spatial dimensions, Phys. Rev. Lett. **101**, 250602 (2008).

[14] H. J. Liao, Z. Y. Xie, J. Chen, Z. Y. Liu, H. D. Xie, R. Z. Huang, B. Normand, and T. Xiang, Gapless spin-liquid ground state in the $S = 1/2$ Kagome anti-ferromagnet, Phys. Rev. Lett. **118**, 137202 (2017).

[15] T. Picot, M. Ziegler, R. Orús, and D. Poilblanc, Spin-S Kagome quantum anti-ferromagnets in a field with tensor networks, Phys. Rev. B **93**, 060407 (2016).

[16] T. Picot and D. Poilblanc, Nematic and supernematic phases in Kagome quantum anti-ferromagnets under the influence of a magnetic field, Phys. Rev. B **91**, 064415 (2015).

[17] A. Kshetrimayum, T. Picot, R. Orús, and D. Poilblanc, Spin-$\frac{1}{2}$ Kagome XXZ model in a field: Competition between lattice nematic and solid orders, Phys. Rev. B **94**, 235146 (2016).

[18] C. Boos, S. P. G. Crone, I. A. Niesen, P. Corboz, K. P. Schmidt, and F. Mila, Competition between intermediate plaquette phases in $SrCu_2(BO_3)_2$ under pressure, Phys. Rev. B **100**, 140413(R) (2019).

[19] A. Kshetrimayum, C. Balz, B. Lake, and J. Eisert, Tensor network investigation of the double layer Kagome compound $Ca_{10}Cr_7O_{28}$, Ann. Phys. **421**, 168292 (2020).

[20] N. Astrakhantsev, F. Ferrari, N. Niggemann, T. Müller, A. Chauhan, A. Kshetrimayum, P. Ghosh, N. Regnault, R. Thomale, J. Reuther, T. Neupert, and Y. Iqbal, Pinwheel valence bond crystal ground state of the spin-$\frac{1}{2}$ Heisenberg anti-ferromagnet on the Shuriken lattice, Phys. Rev. B **104**, L220408 (2021).

[21] A. Kshetrimayum, H. Weimer, and R. Orús, A simple tensor network algorithm for two-dimensional steady states, Nat. Commun. **8**, 1291 (2017).

[22] P. Czarnik, J. Dziarmaga, and P. Corboz, Time evolution of an infinite projected entangled pair state: An efficient algorithm, Phys. Rev. B **99**, 035115 (2019).

[23] C. Hubig and J. I. Cirac, Time-dependent study of disordered models with infinite projected entangled pair states, SciPost Phys. **6**, 031 (2019).

[24] A. Kshetrimayum, M. Goihl, and J. Eisert, Time evolution of many-body localized systems in two spatial dimensions, Phys. Rev. B **102**, 235132 (2020).

[25] A. Kshetrimayum, M. Goihl, D. M. Kennes, and J. Eisert, Quantum time crystals with programmable disorder in higher dimensions, Phys. Rev. B **103**, 224205 (2021).

[26] J. Dziarmaga, Time evolution of an infinite projected entangled pair state: Neighborhood tensor update, Phys. Rev. B **104**, 094411 (2021).

[27] J. Dziarmaga, Time evolution of an infinite projected entangled pair state: A gradient tensor update in the tangent space, Phys. Rev. B **106**, 014304 (2022).

[28] P. Czarnik, L. Cincio, and J. Dziarmaga, Projected entangled pair states at finite temperature: Imaginary time evolution with ancillas, Phys. Rev. B **86**, 245101 (2012).

[29] P. Czarnik and J. Dziarmaga, Variational approach to projected entangled pair states at finite temperature, Phys. Rev. B **92**, 035152 (2015).

[30] A. Kshetrimayum, M. Rizzi, J. Eisert, and R. Orús, Tensor network annealing algorithm for two-dimensional thermal states, Phys. Rev. Lett. **122**, 070502 (2019).

[31] P. Czarnik, A. Francuz, and J. Dziarmaga, Tensor network simulation of the Kitaev-Heisenberg model at finite temperature, Phys. Rev. B **100**, 165147 (2019).

[32] P. Czarnik, M. M. Rams, P. Corboz, and J. Dziarmaga, Tensor network study of the $m = 1/2$ magnetization plateau in the Shastry-Sutherland model at finite temperature, Phys. Rev. B **103**, 075113 (2021).

[33] S. Mondal, A. Kshetrimayum, and T. Mishra, Two-body repulsive bound pairs in a multibody interacting Bose-Hubbard model, Phys. Rev. A **102**, 023312 (2020).

[34] W. Li, S.-J. Ran, S.-S. Gong, Y. Zhao, B. Xi, F. Ye, and G. Su, Linearized tensor renormalization group algorithm for the calculation of thermodynamic properties of quantum lattice models, Phys. Rev. Lett. **106**, 127202 (2011).

[35] Y.-L. Dong, L. Chen, Y.-J. Liu, and W. Li, Bilayer linearized tensor renormalization group approach for thermal tensor networks, Phys. Rev. B **95**, 144428 (2017).

[36] B.-B. Chen, Y.-J. Liu, Z. Chen, and W. Li, Series-expansion thermal tensor network approach for quantum lattice models, Phys. Rev. B **95**, 161104(R) (2017).

[37] B.-B. Chen, L. Chen, Z. Chen, W. Li, and A. Weichselbaum, Exponential thermal tensor network approach for quantum lattice models, Phys. Rev. X **8**, 031082 (2018).

[38] L. Chen, D.-W. Qu, H. Li, B.-B. Chen, S.-S. Gong, J. von Delft, A. Weichselbaum, and W. Li, Two-temperature scales in the triangular-lattice Heisenberg antiferromagnet, Phys. Rev. B **99**, 140404(R) (2019).

[39] H. Li, Y. D. Liao, B.-B. Chen, X.-T. Zeng, X.-L. Sheng, Y. Qi, Z. Yang Meng, and W. Li, Kosterlitz-Thouless melting of magnetic order in the triangular quantum Ising material $TmMgGaO_4$, Nat. Commun. **11**, 1111 (2020).

[40] H. C. Jiang, Z. Y. Weng, and T. Xiang, Accurate determination of tensor network state of quantum lattice models in two dimensions, Phys. Rev. Lett. **101**, 090603 (2008).

[41] O. Gauthé and F. Mila, Thermal Ising transition in the spin-$1/2J_1$-J_2 Heisenberg model, Phys. Rev. Lett. **128**, 227202 (2022).

[42] A. H. Werner, D. Jaschke, P. Silvi, M. Kliesch, T. Calarco, J. Eisert, and S. Montangero, Positive tensor network approach for simulating open quantum many-body systems, Phys. Rev. Lett. **116**, 237201 (2016).

[43] X. Chen, S.-J. Ran, T. Liu, C. Peng, Y.-Z. Huang, and G. Su, Thermodynamics of spin-1/2 Kagomé Heisenberg anti-ferromagnet: algebraic paramagnetic liquid and finite-temperature phase diagram, Sci. Bull. **63**, 1545 (2018).

[44] Z. Y. Xie, J. Chen, J. F. Yu, X. Kong, B. Normand, and T. Xiang, Tensor renormalization of quantum many-body systems using projected entangled simplex states, Phys. Rev. X **4**, 011025 (2014).

[45] T. Nishino and K. Okunishi, Corner transfer matrix renormalization group method, J. Phys. Soc. Jpn. **65**, 891 (1996).

[46] R. Orús and G. Vidal, Simulation of two-dimensional quantum systems on an infinite lattice revisited: Corner transfer matrix for tensor contraction, Phys. Rev. B **80**, 094403 (2009).

[47] R. Orús, Exploring corner transfer matrices and corner tensors for the classical simulation of quantum lattice systems, Phys. Rev. B **85**, 205117 (2012).

[48] S. Sachdev, Kagome- and triangular-lattice Heisenberg anti-ferromagnets: Ordering from quantum fluctuations and quantum-disordered ground states with unconfined bosonic spinons, Phys. Rev. B **45**, 12377 (1992).

[49] Y. Ran, M. Hermele, P. A. Lee, and X.-G. Wen, Projected-wave-function study of the spin-1/2 Heisenberg model on the Kagomé lattice, Phys. Rev. Lett. **98**, 117205 (2007).

[50] H. C. Jiang, Z. Y. Weng, and D. N. Sheng, Density matrix renormalization group numerical study of the Kagome antiferromagnet, Phys. Rev. Lett. **101**, 117203 (2008).

[51] H.-C. Jiang, Z. Wang, and L. Balents, Identifying topological order by entanglement entropy, Nat. Phys. **8**, 902 (2012).

[52] O. Götze, D. J. J. Farnell, R. F. Bishop, P. H. Y. Li, and J. Richter, Heisenberg anti-ferromagnet on the kagome lattice with arbitrary spin: A higher-order coupled cluster treatment, Phys. Rev. B **84**, 224428 (2011).

[53] Y. Iqbal, F. Becca, S. Sorella, and D. Poilblanc, Gapless spin-liquid phase in the Kagome spin-$\frac{1}{2}$ Heisenberg antiferromagnet, Phys. Rev. B **87**, 060405(R) (2013).

[54] A. M. Läuchli, J. Sudan, and R. Moessner, $S = \frac{1}{2}$ Kagome Heisenberg anti-ferromagnet revisited, Phys. Rev. B **100**, 155142 (2019).

[55] H. Schlüter, J. Richter, and J. Schnack, Melting of magnetization plateaus for Kagomé and square-Kagomé lattice anti-ferromagnets, J. Phys. Soc. Jpn. **91**, 094711 (2022).

[56] J. Schnack, J. Schulenburg, and J. Richter, Magnetism of the $N = 42$ Kagome lattice antiferromagnet, Phys. Rev. B **98**, 094423 (2018).

[57] C. Balz, B. Lake, A. T. M. Nazmul Islam, Y. Singh, J. A. Rodriguez-Rivera, T. Guidi, E. M. Wheeler, G. G. Simeoni, and H. Ryll, Magnetic Hamiltonian and phase diagram of the quantum spin liquid $Ca_{10}Cr_7O_{28}$, Phys. Rev. B **95**, 174414 (2017).

[58] R. Pohle, H. Yan, and N. Shannon, Theory of $Ca_{10}Cr_7O_{28}$ as a bilayer breathing-Kagome magnet: Classical thermodynamics and semiclassical dynamics, Phys. Rev. B **104**, 024426 (2021).

[59] S. Trotzky, Y.-A. Chen, A. Flesch, I. P. McCulloch, U. Schollwöck, J. Eisert, and I. Bloch, Probing the relaxation towards equilibrium in an isolated strongly correlated one-dimensional Bose gas, Nat. Phys. **8**, 325 (2012).

[60] D. Hangleiter and J. Eisert, Computational advantage of quantum random sampling, Rev. Mod. Phys. **95**, 035001 (2023).

[61] F. Pan and P. Zhang, Simulation of quantum circuits using the big-batch tensor network method, Phys. Rev. Lett. **128**, 030501 (2022).

[62] Y. Zhou, E. M. Stoudenmire, and X. Waintal, What limits the simulation of quantum computers? Phys. Rev. X **10**, 041038 (2020).

[63] J. Tindall, M. Fishman, M. Stoudenmire, and D. Sels, Efficient tensor network simulation of IBM's Eagle kicked Ising experiment, PRX Quantum **5**, 010308 (2024).

[64] H.-J. Liao, K. Wang, Z.-S. Zhou, P. Zhang, and T. Xiang, Simulation of IBM's kicked Ising experiment with projected entangled pair operators, arXiv:2308.03082.

[65] S. Patra, S. S. Jahromi, S. Singh, and R. Orus, Efficient tensor network simulation of IBM's largest quantum processors, Phys. Rev. Res. **6**, 013326 (2024).

[66] Y. Kim *et al.*, Nature (London) **618**, 500 (2023).

[67] Y. H. Matsuda, N. Abe, S. Takeyama, H. Kageyama, P. Corboz, A. Honecker, S. R. Manmana, G. R. Foltin, K. P. Schmidt, and F. Mila, Magnetization of $SrCu_2(BO_3)_2$ in ultrahigh magnetic fields up to 118 T, Phys. Rev. Lett. **111**, 137204 (2013).

[68] P. Corboz and F. Mila, Crystals of bound states in the magnetization plateaus of the Shastry-Sutherland model, Phys. Rev. Lett. **112**, 147203 (2014).

[69] J. Haah, R. Kothari, and E. Tang, Learning quantum Hamiltonians from high-temperature Gibbs states and real-time evolutions, Nat. Phys. (2024).

[70] A. Anshu, S. Arunachalam, T. Kuwahara, and M. Soleimanifar, Sample-efficient learning of quantum many-body systems, Nat. Phys. **17**, 931 (2021).

[71] F. Wilde, A. Kshetrimayum, I. Roth, D. Hangleiter, R. Sweke, and J. Eisert, Scalably learning quantum many-body Hamiltonians from dynamical data, arXiv:2209.14328.

[72] L. Bennett, B. Melchers, and B. Proppe, Curta: A general-purpose high-performance computer at ZEDAT, Freie Universität Berlin, http://dx.doi.org/10.17169/refubium-26754 (2020).

[73] S. Singh, R. N. C. Pfeifer, and G. Vidal, Tensor network decompositions in the presence of a global symmetry, Phys. Rev. A **82**, 050301(R) (2010).

[74] P. Schmoll, S. Singh, M. Rizzi, and R. Orús, A programming guide for tensor networks with global SU(2) symmetry, Ann. Phys. **419**, 168232 (2020).

[75] N. Schuch, M. M. Wolf, F. Verstraete, and J. I. Cirac, Computational complexity of projected entangled pair states, Phys. Rev. Lett. **98**, 140506 (2007).

[76] J. Haferkamp, D. Hangleiter, J. Eisert, and M. Gluza, Contracting projected entangled pair states is average-case hard, Phys. Rev. Res. **2**, 013010 (2020).

[77] H. N. Phien, J. A. Bengua, H. D. Tuan, P. Corboz, and R. Orús, Infinite projected entangled pair states algorithm improved: Fast full update and gauge fixing, Phys. Rev. B **92**, 035142 (2015).